Structural, magnetic, and spin dynamical properties of the polar antiferromagnets Ni₃₋ₓCoₓTeO₆ (x = 1, 2)

Stella Skiadopoulou [1,2,3,*] Maria Retuerto,[4] Fedir Borodavka [1] Christelle Kadlec,[1] Filip Kadlec [1] Martin Míšek,[1]
Jan Prokleška,[5] Zheng Deng,[4] Xiaoyan Tan,[4,†] Corey Frank [4] Jose A. Alonso [6] Maria Tereza Fernandez-Diaz,[7]
Mark Croft,[8] Fabio Orlandi,[9] Pascal Manuel,[9] Emma McCabe [10] Dominik Legut,[2]
Martha Greenblatt,[4] and Stanislav Kamba [1]

[1]*Institute of Physics,Czech Academy of Sciences, Na Slovance 2, 18221 Prague 8, Czech Republic*
[2]*IT4Innovations, VSB Technical University of Ostrava, 17, Listopadu 2172/15, CZ-708 00 Ostrava-Poruba, Czech Republic*
[3]*School of Physics, CRANN, Trinity College, Dublin 2, Ireland*
[4]*Department of Chemistry and Chemical Biology, Rutgers, The State University of New Jersey, 610 Taylor Road, Piscataway, New Jersey 08854, USA*
[5]*Department of Condensed Matter Physics, Faculty of Mathematics and Physics, Charles University, Ke Karlovu 5, 121 16 Prague 2, Czech Republic*
[6]*Instituto de Ciencia de Materiales de Madrid, C.S.I.C., Cantoblanco, E-28049 Madrid, Spain*
[7]*Institut Laue Langevin, BP 156X, Grenoble, F-38042, France*
[8]*Department of Physics and Astronomy, Rutgers, the State University of New Jersey, 136 Frelinghusen Road, Piscataway, New Jersey 08854, USA*
[9]*ISIS Facility, STFC, Rutherford Appleton Laboratory, Chilton, Didcot, Oxfordshire, OX11 0QX, United Kingdom*
[10]*School of Physical Sciences, University of Kent, Canterbury, Kent, CT2 7NH, United Kingdom*

We present results of a multimethod investigation of the polar antiferromagnets Ni₂CoTeO₆ and NiCo₂TeO₆, inspired by the colossal magnetoelectric effect present in Ni₃TeO₆. Both compounds crystalize in the same polar space group $R3$ as Ni₃TeO₆, preserving the crystal symmetry at least from room temperature down to 2 K. Ni₂CoTeO₆ and NiCo₂TeO₆ undergo antiferromagnetic phase transitions at $T_N = 55$ and 52 K, and spin-flop transitions at an external magnetic field of approximately 8 and 4 T, respectively. Both compounds present an incommensurate antiferromagnetic helical structure with spins lying in the ab plane, in contrast to the collinear one along the c axis in Ni₃TeO₆. Moreover, dielectric anomalies are observed at their antiferromagnetic phase transitions, suggesting a magnetoelectric behavior. Spin and lattice dynamics studies by a combination of infrared, Raman, and terahertz spectroscopies were performed. Below T_N, in both Ni₂CoTeO₆ and NiCo₂TeO₆, low-frequency spin excitations extremely sensitive to external magnetic field were observed. At least one of these magnons was simultaneously seen in Raman and THz spectra of both compounds, therefore we propose to assign them to electromagnons.

I. INTRODUCTION

The polar antiferromagnet Ni₃TeO₆ exhibits static (colossal) [1] and dynamical [2] magnetoelectric (ME) effects. A collinear antiferromagnetic (AFM) order appears below the Néel temperature $T_N = 53$ K [3], giving rise to spin-induced polarization of up to 3280 μC/m² (at 2 K) [1]. Two spin excitations observed simultaneously in Raman and time-domain THz spectra emerge below T_N [2]. These magnons show high tunability in external magnetic field. Due to symmetry considerations, these excitations are assigned to electromagnons, i.e., electrically active magnons [2,4,5]. Since Ni₃TeO₆ presents a collinear AFM spin structure, the spin-lattice coupling mechanism (symmetric exchange striction) is

most probably responsible for the emergent dynamical ME effect. A similar polar antiferromagnet Ni₂MnTeO₆, undergoes an AFM phase transition at $T_N \approx 70$ K, almost 20 K higher than Ni₃TeO₆, while keeping the same polar rhombohedral $R3$ space group symmetry [6]. A dielectric anomaly at T_N suggests a ME behavior, and a magnetic field-sensitive spin excitation appears below T_N in the THz range.

The cryolite-related Co₃TeO₆ with the monoclinic $C2/c$ space group symmetry down to 1.9 K [7] undergoes at least three magnetic phase transitions within the range from 26 to 16 K [7–13]. Two main competing reports on the complex magnetic ordering in Co₃TeO₆ suggest either switching from an incommensurate collinear AFM (∼26 K) to a commensurate noncollinear AFM structure (∼17 K) with multiple propagation vectors [7,10], or a coexistence of two layers with commensurate collinear and incommensurate noncollinear AFM spin orderings [12]. In the lowest temperature phase, a magnetically induced polarization of up to 160 μC/m² ($P \parallel c$, $H \parallel a$, 5 K, 9 T) emerges [7,8], possibly via the spin-current mechanism (antisymmetric exchange) [11].

---

*Corresponding author: skiadops@tcd.ie
†Present address: Department of Chemistry and Biochemistry, George Mason University, 4400 University Dr, Fairfax, Virginia 22030, USA.

The peculiar magnetoelectricity and complex magnetic ordering of Co_3TeO_6, in combination with the colossal magnetoelectric coupling in Ni_3TeO_6, led to the concept of Ni substitution by Co in Ni_3TeO_6. For the current study, Ni_2CoTeO_6 and $NiCo_2TeO_6$ were synthesized in the form of single crystals and polycrystalline samples. Partial Ni substitution by Co preserves the polar $R3$ crystal symmetry of Ni_3TeO_6, while inducing a noncollinear helical spin structure, in contrast to the collinear cases of Ni_3TeO_6 and Ni_2MnTeO_6. The helical spin configurations in Ni_2CoTeO_6 and $NiCo_2TeO_6$ yield hysteretic spin-flop transitions; in comparison, spin-flop transitions in the collinear cases are nonhysteretic. In this article, we discuss spin and lattice excitations with an emphasis on the magnetic-field sensitive magnons in the THz range.

II. EXPERIMENTAL SECTION

Polycrystalline Ni_2CoTeO_6 and $NiCo_2TeO_6$ were prepared by solid state reactions. Stoichiometric amounts of NiO, TeO_2, and $MnCO_3$ were mixed, ground together, and heated in a tubular furnace under oxygen flux at 800 °C with intermediate grindings between 700 and 800 °C.

Single crystals of both materials were prepared by the flux method by mixing the corresponding mixed oxide (Ni_2CoTeO_6 or $NiCo_2TeO_6$) with V_2O_5, TeO_2, NaCl, and KCl in a molar ratio of the five compounds of 1:5:10:10:5. The mixture was heated to 830 °C and kept at this temperature during three days. The crystals were cooled to 600 °C during five days. Plate-shaped crystals were obtained with lateral dimensions of ~2 mm for Ni_2CoTeO_6 and less than 1 mm for $NiCo_2TeO_6$. (See Fig. S1.1 in the Supplemental Material (SM) [14], see also Refs. [15–19] therein).

The samples were initially characterized by powder x-ray diffraction (XRD) (Cu $K_\alpha = 1.5406$ Å). The structure of the single crystals was determined by single-crystal x-ray data collected on a Bruker Smart APEX CCD diffractometer with graphite-monochromatized Mo K_α radiation ($\lambda = 0.71073$ Å) at 100 K.

Time-of-flight neutron powder diffraction (NPD) data were collected for $NiCo_2TeO_6$ on the WISH diffractometer (target station 2) at the ISIS neutron and muon source [20]; ~250 mg of powder were placed in a thin-walled, cylindrical vanadium can and cooled to 1.5 K. High quality data sets with angular steps equivalent to 40 μÅ in direct space were collected at 1.5, 32, and 60 K. Shorter scans with finer steps of 6.7 μÅ were collected at intermediate temperatures, and the data at 100 K were obtained with 16.8 μÅ steps. Constant wavelength NPD data were collected for Ni_2CoTeO_6; 250 mg of powder were placed in a 6- mm-diameter vanadium can. High resolution scans were collected on the D2B diffractometer ($\lambda \approx 1.59$ Å) at 1.5 and 300 K. Variable temperature data were also collected on the high flux diffractometer D20 ($\lambda \approx 2.41$ Å) to follow the magnetic ordering.

TOPASACADEMIC [21] software was used for initial refinements using data collected in the paramagnetic region to determine the Ni/Co distribution over $3a$ sites. The cation distribution was then fixed for refinements using Jana2006 [22] using data collected at base temperature and on warming. Group theory calculations and magnetic symmetry analysis

were performed with the help of the ISODISTORT and ISOTROPY software [23,24].

Radio-frequency dielectric measurements were performed using a NOVOCONTROL α-AN impedance analyzer in conjunction with a JANIS ST-100 cryostat.

Near-normal incidence infrared (IR) reflectivity spectra of $Ni_{3-x}Co_xTeO_6$ ($x = 1, 2$) ceramics were measured using a Fourier-transform IR spectrometer Bruker IFS 113v in the frequency range of $20-3000\,cm^{-1}$ (0.6–90 THz) at room temperature; the low-temperature spectral range was reduced to $20-650\,cm^{-1}$ due to the limited transparency of the cryostat windows from polyethylene. A pyroelectric deuterated triglycine sulfate detector was used for the room-temperature measurements, whereas a He-cooled (operating temperature 1.6 K) Si bolometer was used for the low-temperature measurements down to 7 K.

Time-domain terahertz experiments were conducted in the spectral range from 3 to $60\,cm^{-1}$ (0.09–1.8 THz), performed in the transmission geometry with a custom-made time-domain terahertz spectrometer. A train of femtosecond pulses was produced by a femtosecond Ti:sapphire laser oscillator (Coherent, Mira), which generated linearly polarized broadband THz pulses radiated by a photoconducting switch TeraSED (Giga-Optics). A gated detection scheme based on electro-optic sampling with a 1-mm-thick [110] ZnTe crystal as a sensor allowed us to measure the time profile of the electric field of the transmitted THz pulse. For low-temperature THz and IR measurements, two Oxford Instruments Optistat cryostats with mylar and polyethylene windows, respectively, were used. External magnetic field THz experiments with $\mu_o H_{ext} \leqslant 7\,T$ were conducted with an Oxford Instruments Spectromag cryostat in the Voigt configuration (with both $\boldsymbol{H}_{ext} \parallel \boldsymbol{E}^\omega$ and $\boldsymbol{H}_{ext} \perp \boldsymbol{E}^\omega$), where $\boldsymbol{E}^\omega$ denotes the electrical component of the electromagnetic radiation.

The IR reflectivity $R(\omega)$ and THz complex permittivity $\varepsilon(\omega)$ spectra were fitted assuming a sum of N independent damped harmonic oscillators, expressed as [25]

$$\varepsilon(\omega) = \varepsilon_\infty + \sum_{j=1}^{N} \frac{\Delta\varepsilon_j \omega_{TOj}^2}{\omega_{TOj}^2 - \omega^2 + i\omega\gamma_{TOj}}, \qquad (1)$$

where $\Delta\varepsilon_j$ is the dielectric strength of the jth mode, ω_{TOj} are the frequencies of the jth transverse optical (TO) phonons, and γ_{TOj} are the corresponding damping constants. ε_∞ is the high-frequency (electronic) contribution to the permittivity, determined from the room-temperature frequency-independent reflectivity tail above the phonon frequencies. The complex magnetic permeability μ may be expressed in a similar way, and then the reflectivity, the complex dielectric function and the complex magnetic permeability are related by

$$R(\omega) = \left| \frac{\sqrt{\varepsilon(\omega)} - 1}{\sqrt{\varepsilon(\omega)} + 1} \right|^2, \quad R(\omega) = \left| \frac{\sqrt{\varepsilon} - \sqrt{\mu}}{\sqrt{\varepsilon} + \sqrt{\mu}} \right|^2. \quad (2)$$

Raman studies of single crystals were performed with a Renishaw RM 1000 Micro-Raman spectrometer with Bragg filters, equipped with an Oxford Instruments Microstat continuous-flow optical He cryostat. The experiments were conducted in the backscattering geometry in the

$5-1800\,cm^{-1}$ range. An Ar^+-ion laser operating at 514.5 nm was used. The spectra were carefully fit with a sum of independent damped harmonic oscillators multiplied by the corresponding Stokes temperature factor [26].

III. RESULTS AND DISCUSSION

A. Structural characterization

Single crystals and polycrystalline samples of Ni_2CoTeO_6 and $NiCo_2TeO_6$ were characterized by XRD and NPD, revealing pure phases with the noncentrosymmetric $R3$ space group symmetry. The XRD and NPD patterns, unit cell parameters, atomic positions, and bond distances, are presented in Secs. S2 and S3 in the SM [14]. Both compounds present layers of edge-sharing NiO_6, CoO_6, and TeO_6 octahedra, where the central Ni, Co, and Te ions are slightly (by ~ 0.1 Å) displaced from the centers of the oxygen octahedra cages.

B. Magnetic structures

The magnetic structures of both compounds, determined by NPD, correspond to an incommensurate AFM helical with the magnetic moments lying in the ab plane, in clear contrast with the collinear out-of-plane spin structure of Ni_3TeO_6 and Ni_2MnTeO_6 [1,3,6]. The magnetic propagation vectors are $\boldsymbol{k}_1 = (0, 0, 1.299(4))$ and $\boldsymbol{k}_2 = (0, 0, 1.2109(1))$, for Ni_2CoTeO_6 and $NiCo_2TeO_6$ at 3 and 1.5 K, respectively. In both compounds the magnetic structure is described by the superspace group $R31'(00\gamma)ts$, corresponding to the mΛLE2 irreducible representation. The helical structure is characterized by ferromagnetic (FM) ab layers rotating along the c axis (Fig. 1) yielding an AFM structure. It is interesting to note that the sole difference between the two compounds is the periodicity of the helix along c, which increases with Co^{2+} content approaching $k = (0\,0\,\frac{3}{2})$. The incommensurate nature of the magnetic structures suggests some frustration in magnetic exchanges along the c axis and a lack of a clear anisotropy direction in the ab plane. Details of the structure refinements, Rietveld plots, values of the magnetic moments as well as the temperature evolutions of the magnetic structures are reported in Sec. S3 in the Supplemental Material [14].

Note that the related materials $Ni_{2-x}Co_xScSbO_6$ ($x = 0-1.5$) and Mn_2InSbO_6 have similar polar $R3$ crystal structures, but their magnetic structures differ substantially. The helical spin structure of Ni_2ScSbO_6 is incommensurately modulated with an in-plane propagation vector $\boldsymbol{k} = [0\,0.036(1)\,0]$, corresponding to an almost 40 times longer helix than that in the $Ni_{3-x}Co_xTeO_6$ compounds [27]. With the addition of Co, the $Ni_{2-x}Co_xScSbO_6$ ($x = 0.5-1.5$) compounds present a series of long-periodicity commensurate helices with $\boldsymbol{k} = [0\,0\,1/3n]$, where $n = 5$, 6, 8 and 10 for $x = 0.5$, 1, 1.5, and 2, thus the helix length increases with increasing Co contents [28].

Finally, the double-corundum compound Mn_2InSbO_6 exhibits three magnetic phase transitions below 38 K, and the structure may exhibit a commensurately modulated helix with a propagation vector $\boldsymbol{k} = [0\,0\,0]$, an incommensurate one with $\boldsymbol{k} = [0\,0\,k_z]$, or a commensurate one with $k_z = 1/8$ [29].

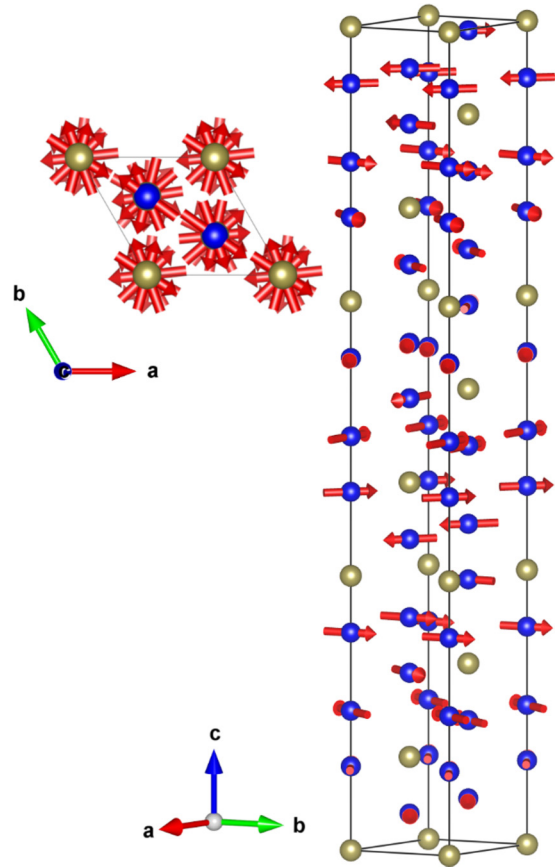FIG. 1. Schematic representation of the incommensurate helical magnetic structure of Ni_2CoTeO_6 and $NiCo_2TeO_6$ (the magnetic Ni/Co sites are presented as blue spheres, whereas Te atoms are shown in gold, oxygen atoms are not shown for clarity). The magnetic structures of both compounds are quite similar, with a small difference between the magnetic propagation vectors: $k_1 = (0, 0, 1.299(4))$ and $k_2 = (0, 0, 1.2109(1))$, for Ni_2CoTeO_6 and $NiCo_2TeO_6$, respectively.

C. Magnetic and dielectric properties

The temperature dependences of the magnetization in Ni_2CoTeO_6 and $NiCo_2TeO_6$ polycrystalline samples reveal AFM phase transitions at 54 and 49 K, respectively [Fig. 2(a)]. Similarly, the single crystals of Ni_2CoTeO_6 and $NiCo_2TeO_6$ exhibit AFM orderings at slightly higher temperatures of 55 and 52 K, respectively [Figs. S2(a) and S2(b) in the SM] [14]. Here we chose to show the results of the ceramic samples, in order to provide a comparison with the dielectric measurements done exclusively on ceramics.

The magnetic transitions in both samples resemble that of Ni_3TeO_6, unlike Ni_2MnTeO_6, which orders antiferromagnetically at around 70 K [6]. The single crystals were measured after applying 0.1 T, at zero field cooling, and for two different magnetic field configurations: $\boldsymbol{H}_{ext} \parallel c$ axis and $\boldsymbol{H}_{ext} \parallel ab$ plane. In contrast to Ni_2MnTeO_6 exhibiting a c-easy-axis magnetization, both Co compounds present ab-easy-plane magnetization, confirming the magnetic structure indicated by the NPD experiments. An additional anomaly at around 35 K is present in the Ni_2CoTeO_6 single crystal [Fig. S5(a) in the SM] [14], possibly due to another magnetic phase transition.
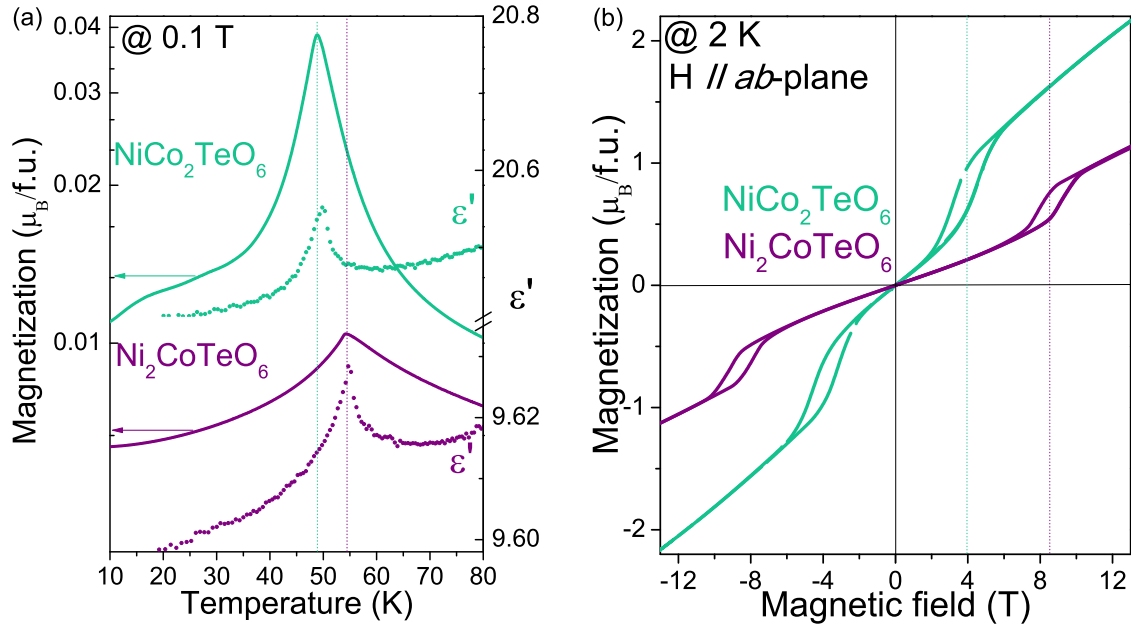
FIG. 2. (a) Temperature dependences of magnetization (at 0.1 T; logarithmic scale) and permittivity (at 0.1 MHz) for Ni_2CoTeO_6 and $NiCo_2TeO_6$ ceramics, presenting AFM phase transition at 54 and 49 K, respectively. The dielectric anomalies also appear at the same temperatures for each compound. (b) Magnetic field dependences of magnetization with $H_{ext} \parallel ab$ plane at 2 K for Ni_2CoTeO_6 and $NiCo_2TeO_6$ single crystals, revealing spin flop transitions at approximately 8 and 4 T, respectively.

The same anomaly is absent in the ceramic samples (neither was it observed in NPD), due to random orientations of the grains. As anticipated due to the multiferroic behavior of Ni_3TeO_6 and Ni_2MnTeO_6, also Ni_2CoTeO_6 and $NiCo_2TeO_6$, there is evidence of an interplay of magnetic and dielectric properties, as indicated by the dielectric anomaly seen at T_N [Fig. 2 (a)]. The critical temperatures amount to 53 and 47 K for Ni_2CoTeO_6 and $NiCo_2TeO_6$ ceramic samples, respectively, slightly lower ($\sim$1–2 K) than the magnetic anomalies. Such a discrepancy, which lies close to the experimental error, may also originate in thermo-lag effect at the sample-thermocouple contact during the measurements. The permittivity values of the two compounds differ, with Ni_2CoTeO_6 close to Ni_3TeO_6 [1], whereas $NiCo_2TeO_6$ presents a twice higher value, thus nearing that of Ni_2MnTeO_6 [6]. However, one may only make a rough comparison between the static permittivity values, since they were measured at different frequencies: 44 kHz, 0.1 MHz, and 1 MHz, for Ni_3TeO_6, Ni_2CoTeO_6/$NiCo_2TeO_6$, and Ni_2MnTeO_6, respectively.

The magnetic field dependences of magnetization of Ni_2CoTeO_6 and $NiCo_2TeO_6$ single crystals at 2 K and for $H_{ext} \parallel ab$ axis are shown in Fig. 2(b). Ni_2CoTeO_6 presents a spin-flop transition at approximately 8 T, similarly to Ni_3TeO_6 [1], however $NiCo_2TeO_6$ exhibits a dramatic decrease in the spin-flop critical field down to about 4 T. Such a behavior can be explained by the helical spin structure (Fig. 1), and by the lack of a strong anisotropy direction of the FM layers in the ab plane. The famous nonhysteretic behavior of Ni_3TeO_6 is absent in both compounds, which manifest a strong hysteresis in the magnetic field-dependent magnetization. The ceramic samples demonstrate similar magnetic phase transitions, albeit at slightly lower values of magnetic field, possibly due to grain boundary contributions (Fig. S3 in the SM) [14]. In

addition, the hysteretic behavior becomes more pronounced for both samples on cooling (see Fig. S5.2).

D. Spin and lattice excitations

The family of the four Ni-based tellurates, Ni_3TeO_6, Ni_2MnTeO_6, Ni_2CoTeO_6 and $NiCo_2TeO_6$, crystalize in the polar $R3$ space group, at least from room temperature (RT) down to 4 K and it is known that Ni_3TeO_6 keeps the same rhombohedral structure up to 1000 K [27]. As expected, all compounds present almost identical vibrational spectra [2,6,18]. All 18 vibrational modes predicted by factor group analysis [$9E(x, y, x^2 - y^2, xy, xz, yz)$ and $9A(x^2 + y^2, z^2, z)$], both IR and Raman active, are present in the IR reflectivity spectra of both compounds [see Figs. 3(a) and 3(d)]. The corresponding mode frequencies are listed in Table S6 in the SM [14]. The anticipated weak temperature dependence of the IR reflectivity spectra of Ni_2CoTeO_6 and $NiCo_2TeO_6$ confirms the resemblance among the four compounds and the stability of the crystal structure in the whole temperature range studied. Naturally, the damping constants of the modes decrease on cooling. In analogy to the mode at $310\,cm^{-1}$ in Ni_3TeO_6, the modes seen in Ni_2CoTeO_6 and $NiCo_2TeO_6$ at 224 and $211\,cm^{-1}$, respectively, exhibit a conspicuous frequency hardening, accompanied by a decrease in damping. The observed phenomenon of mode intensity loss below T_N might be related to a coupling between the phonon and a lower energy magnon. As we show below, both compounds show several spin excitations in the THz range, thus a transfer of dielectric strength from the phonon to a spin excitation may take place when the magnetic ordering occurs and the magnon becomes electrically active (i.e., it contributes to the permittivity), which is a typical signature of electromagnons.
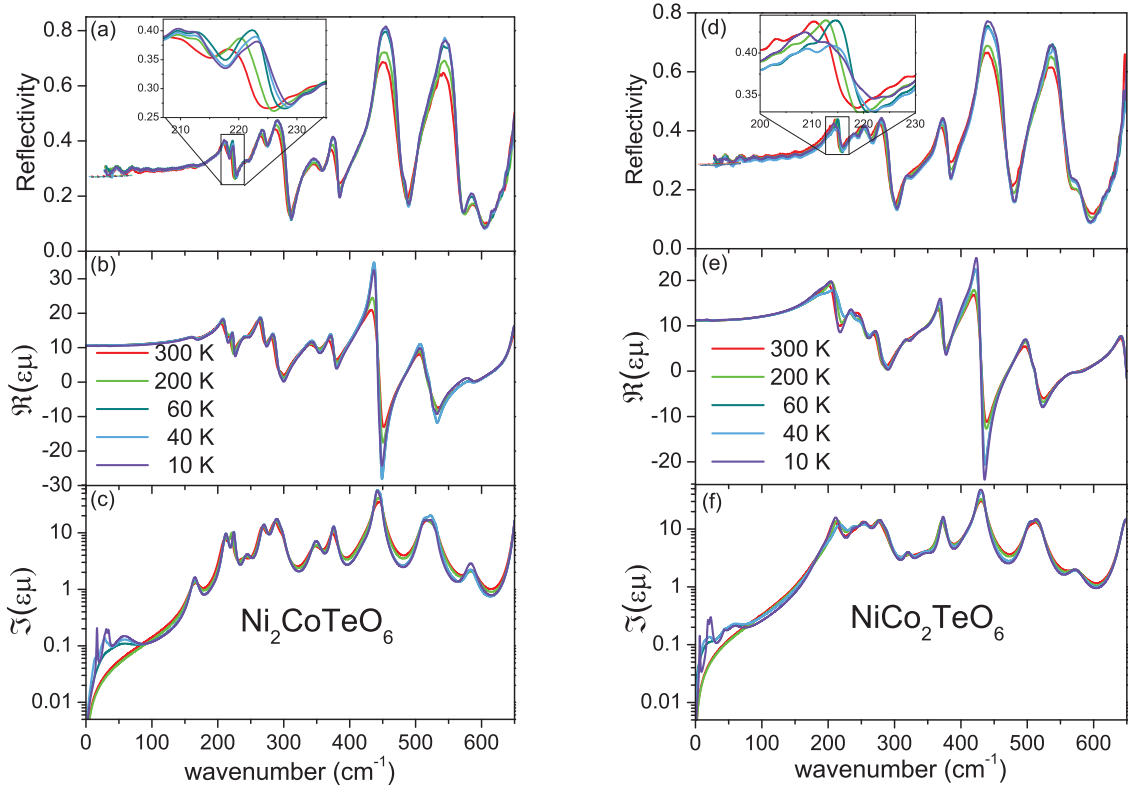
FIG. 3. Temperature dependences of IR reflectivity spectra for (a) Ni_2CoTeO_6 and (d) $NiCo_2TeO_6$ ceramics, at selected temperatures. The reflectivity spectra calculated using the THz range data are also shown, for frequencies below $70\,cm^{-1}$, by dense dotted lines. Insets: Temperature dependences of IR reflectivity of the modes near (a) $220\,cm^{-1}$ and (d) $215\,cm^{-1}$, showing conspicuous decrease in damping on cooling, accompanied by frequency increase. (b), (e) Real and (c), (f) imaginary parts of the product of complex permittivity and complex magnetic permeability, as obtained from the fits.

The spectra were fit assuming a sum of independent harmonic oscillators, as mentioned in Sec. II. The products of the complex permittivity ε and permeability μ spectra obtained by the fits for both compounds are plotted in Figs. 3(b), 3(c), 3(e), and 3(f). Although, the THz spectra are analyzed below in detail, here it is worth mentioning that the IR spectra were fit simultaneously with the THz spectra. In the low-frequency $\Im(\varepsilon\mu)$ spectra [Figs. 3(c) and 3(f)] one can notice weak spin excitations appearing below T_N, as measured by the THz spectroscopy. Since we do not know whether they contribute only to permittivity or permeability, we present their product.

Note that these modes are very weak, therefore they are not visible in the real part of spectra. All the modes seen above $150\,cm^{-1}$ are polar phonons, i.e., they contribute only to permittivity and $\mu' = 1$ in this range.

For both compounds a significant number of sharp modes can be seen in the temperature dependent Raman spectra of single crystals at all possible polarization configurations $[z(xy)\bar{z}, z(xx)\bar{z}, z(yy)\bar{z}, x(yz)\bar{x}, x(yy)\bar{x}, x(zz)\bar{x}]$ taken in the backscattering geometry. Here we present only $z(xy)\bar{z}$ spectra (Fig. 4), where the magnetic excitation is more pronounced comparing to the other configurations.

All above-mentioned configurations measured at 4 K are plotted in Fig. S6 in the SM [14]. The temperature dependence of $x(zy)\bar{x}$, $x(yy)\bar{x}$ and $x(zz)\bar{x}$ polarization configurations for both compounds are presented in the Figs. S6.1.2 and S6.1.3, together with a schematic representation of the configurations

used and their respective Porto notations (Fig. S6.1) in the SM [14]. The Raman modes from all possible polarization configurations for Ni_2CoTeO_6 and $NiCo_2TeO_6$ are listed together with the IR modes in Table S6.2.1 in the SM [14]. Both compounds show an additional mode in the low-frequency range, at approximately $15-16\,cm^{-1}$, which turns up below the AFM transition, therefore we assume it is of magnetic origin. This low frequency excitation appears in most polarization configurations, as seen in the SM [14], however, the strongest intensity corresponds to $z(xy)\bar{z}$, reflecting the ab-plane-sensitivity of the magnon. Note that the observed low-intensity modes observed in other polarized spectra may also originate in polarization leakage, due to slight sample misalignments. In addition, for $x(yz)\overset{'}{x}$ in Ni_2CoTeO_6, a broader mode is seen at around $67\,cm^{-1}$, which might be of two-magnon scattering origin. As we show below in more detail, both modes are also observed in the THz spectra.

The temperature dependence of the imaginary part of the index of refraction in the THz range is shown in Figs. 5(b) and 5(f) for Ni_2CoTeO_6 and $NiCo_2TeO_6$, respectively (ceramics of ~1.9-mm thickness). The real part of the index of refraction for both compounds is presented in Fig. S6.2 in the SM [14]. The spectra were measured from 300 down to 5 K. An initial decrease in the real part of the index of refraction on cooling is observed, followed by the appearance of two modes below T_N for both Ni_2CoTeO_6 ($T_N \approx 54\,K$) and $NiCo_2TeO_6$ ($T_N \approx 49\,K$). All excitations sharpen and harden on cooling,
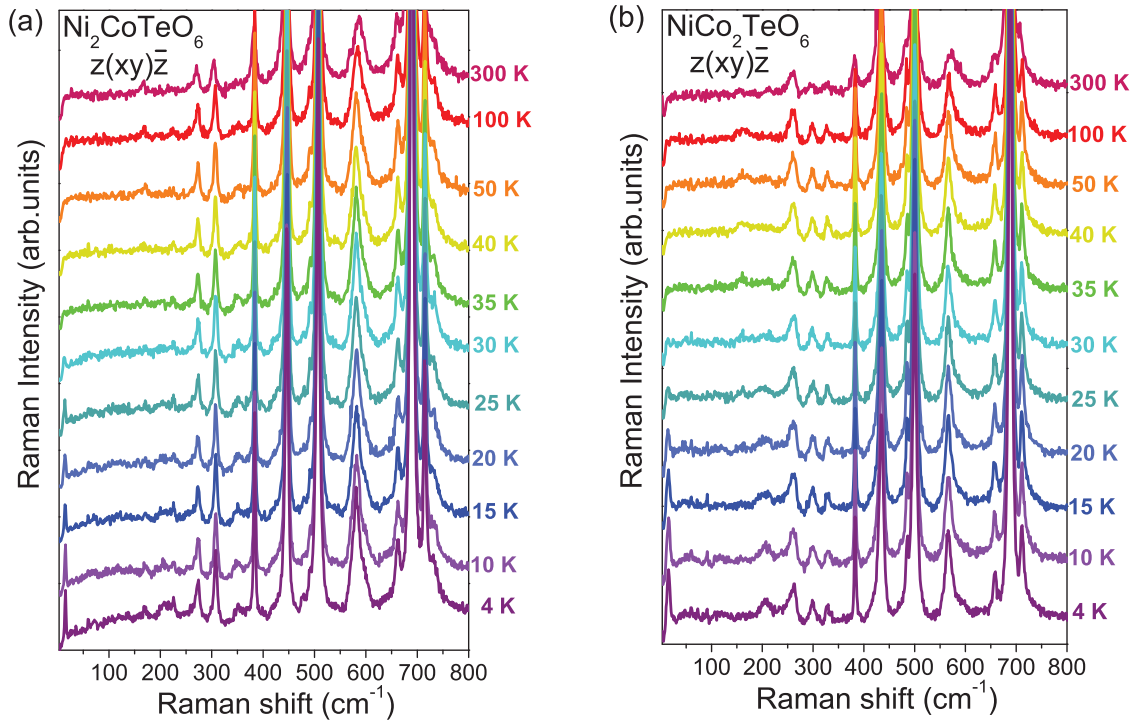
FIG. 4. Temperature dependences of Raman spectra for (a) Ni_2CoTeO_6 and (b) $NiCo_2TeO_6$ single crystals, measured at $z(xy)\bar{z}$ polarization configuration. A spin excitation appears below T_N at $\sim 15\,cm^{-1}$ for both compounds.

with evident splitting for the broader ones. The spectra were fit together with those of IR reflectivity, and the corresponding frequencies, damping constants, and mode strengths are listed in Table S6.2.1 in the SM [14].

At the lowest temperature of 5 K the THz spectrum of Ni_2CoTeO_6 displays five modes, whereas $NiCo_2TeO_6$ presents six of them. The rapid strengthening of these modes upon cooling below T_N, especially of the sharp ones, suggests that they correspond to spin excitations. As mentioned above, the $15\,cm^{-1}$ mode is simultaneously seen in the Raman spectra of both compounds. Magnons are mostly very weak or inactive in Raman spectra. Nevertheless, in some magnetic materials like orthoferrites, the magnons are clearly observed in Raman spectra [30] and they are also IR active, despite their centrosymmetric *Pnma* crystal structure. Ni_2CoTeO_6 and $NiCo_2TeO_6$ have a noncentrosymmetric *R3* crystal structure, so the phonons and magnons can be both IR and Raman active. Since the magnons were observed in the $z(xx)\bar{z}$ and $z(xy)\bar{z}$ Raman spectra, they belong to the E symmetry. As the phonons near $210-220\,cm^{-1}$ reduce their oscillator strengths on cooling below T_N, they probably transfer their dielectric strengths to the strongest Raman-active magnons near $17\,cm^{-1}$ and therefore we assume that these excitations can be called electromagnons. Note the small strengths of all our spin excitations in the THz spectra measured in transmission using a 1.9-mm-thick sample. The broader mode near $60\,cm^{-1}$ (Fig. 3) is also seen in Raman spectra (Figs. S6.1.2 and S6.1.3), but it most probably corresponds to two-magnon scattering.

Spectra of the extinction coefficient obtained by time-domain THz measurements in the Voigt configuration with external magnetic field $H_{ext} \perp E^\omega$ up to 7 T and at temperatures

of 30 and 5 K are presented in Figs. 5(c) and 5(d) and 5(g) and 5(h) for each compound, respectively. The spectra of the real parts of the index of refraction are presented in Fig. S6.2.2 in the SM [14]. In both compounds, the magnons can be tuned by applying external magnetic field, upon which they exhibit noticeable peak sharpening and frequency shifts. The magnetic field dependences of the spin-wave frequencies at 5 K, obtained by the fits, are summarized in Figs. 6(a) and 6(b). In Ni_2CoTeO_6, the sharp mode seen at 30 K around $17\,cm^{-1}$ (0 T) [Fig. 5(c)] softens down to $14\,cm^{-1}$ at 7 T, whereas the higher-frequency modes near $30\,cm^{-1}$ are less sensitive to H_{ext}. The $17\,cm^{-1}$ (0 T) mode was also seen in Raman spectra, as mentioned above. The small discrepancy between the frequencies can be explained by the experimental error and it may also slightly vary in different experimental setups. The sharpening and softening of the latter mode is even more pronounced at 5 K [Fig. 5(d)].

The changes in the magnons response in external magnetic field are even more pronounced in $NiCo_2TeO_6$. At 30 K [Fig. 5(g)], the two strongest modes near 7 and $23\,cm^{-1}$ at 0 T, harden to 13 and $28\,cm^{-1}$, respectively, with rising field up to 7 T. At 5 K the spectra are much richer [Fig. 5(h)]. The magnon frequency shifts due to external magnetic field can be seen in Fig. 6(b). The marked discontinuities that occur at $\sim$4 T in the frequencies of at least four of the excitations, are probably linked to the spin-flop transition, observed also by the magnetization measurements [Fig. 2(b)]. Two new modes seem to appear at around $30\,cm^{-1}$ above 3 T. These new excitations might also correspond to a splitting of the neighboring singlet mode, triggered by the spin-flop transition. The convoluted noncollinear magnetic behavior of the Co-rich compounds was foreseen due to the intriguing
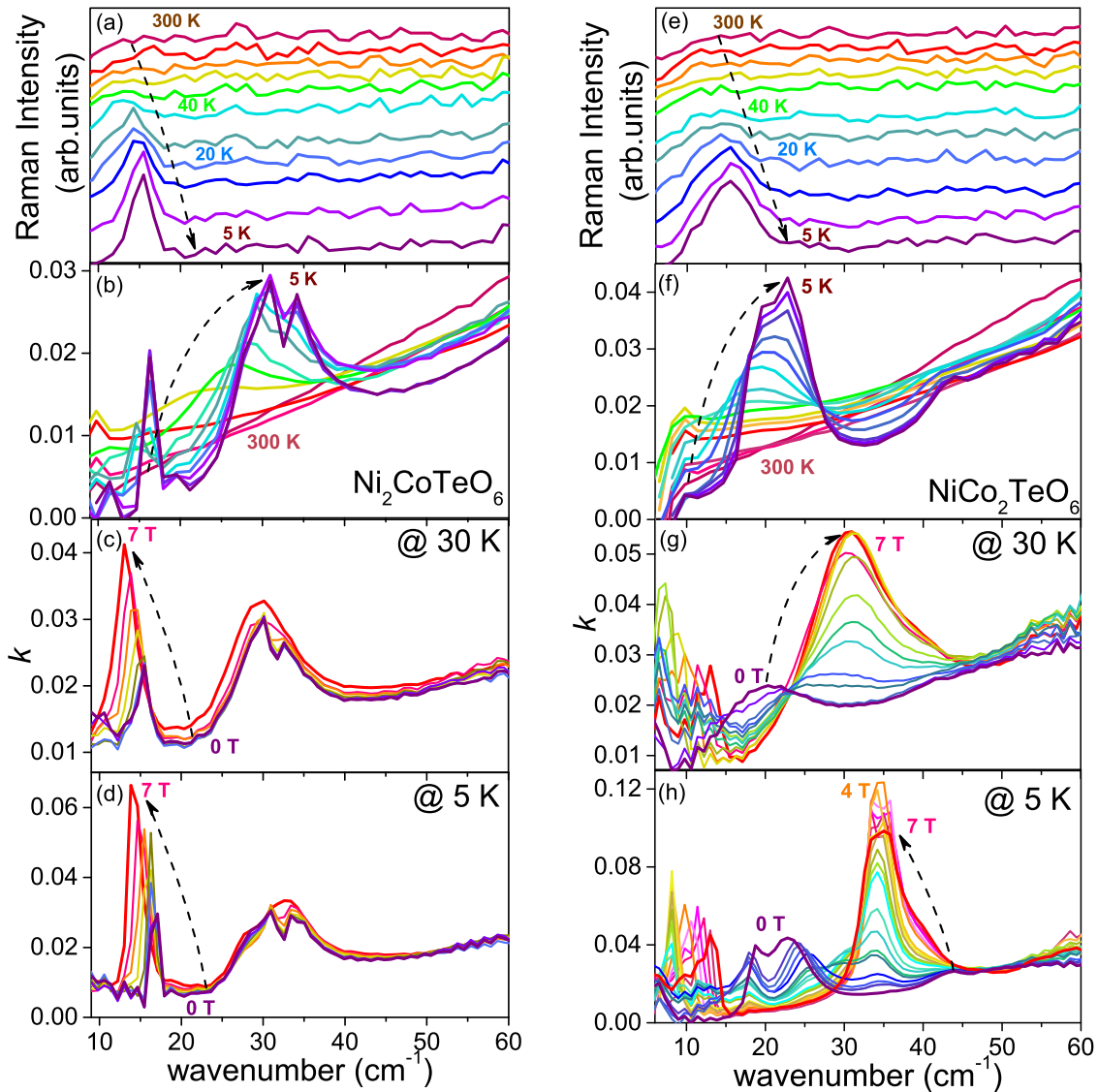
FIG. 5. (a),(e) Temperature dependences of the low frequency $z(xy)\bar{z}$ Raman spectra, (b),(f) temperature and (c),(d),(g),(h) magnetic field dependences of the imaginary part of the index of refraction from THz measurements for Ni_2CoTeO_6 (a)–(d) and $NiCo_2TeO_6$ (e)–(h). At least five spin excitations appear below T_N for both compounds, and the one at $\sim 15\,cm^{-1}$ is simultaneously seen in the Raman spectra. The arrows in parts (a), (b), (e), and (f) indicate the temperature decrease from 300 to 5 K, whereas in (c), (d), (g), and (h), they show the increase of the external magnetic field from 0 to 7 T.

magnetism of Co_3TeO_6 [7,8,10], as well as the spin-orbit coupling contribution from Co^{3+} ($3d$ [6]).

The 15-cm^{-1} mode seen in Raman spectra [Fig. 5(e)], possibly corresponds to the one in the THz spectra at $\sim 17\,cm^{-1}$ (0 T), and it shows a strong magnetic field dependence. Since this mode (together with its higher-frequency component near 22 cm^{-1}) increases its strength below T_N in THz spectra [Fig. 5(f)] and the phonon mode near 215 cm^{-1} reduces its dielectric strength on cooling below T_N (Fig. 3), these modes are probably coupled. It strongly suggests that the spin excitation seen near 17 and 22 cm^{-1} are electrically active and can be called electromagnons.

The discrepancies in the T_N values observed by Raman spectroscopy (the magnetic modes disappear already at ~ 40 K, more than 10 K below the AFM phase transition) could be explained by thermo-lag effects, laser-heating, and/or random crystallite orientation in the polycrystalline samples.

Note that the observed excitations cannot correspond to crystal field splitting caused by the octahedral coordination geometry in Ni, Co, and Te, since the $3d$-related crystal field splitting values lie in the UV and visible range [34], whereas the $4f$-related splitting reaches down to the far-IR range [35].

Substitution of Ni by Mn and Co in the $Ni_{3-x}(Co, Mn)_xTeO_6$ ($x = 0-2$) compound family preserves the polar $R3$ crystal structure. However, the different magnetic anisotropies introduced by the magnetic cations Ni(II)($3d$ [8]), Mn(II)($3d$ [5]) and Co(II)($3d$ [7]) dramatically affect the magnetic phase transitions and the spin order (see Table I). The differences in the spin modulations of the compounds are reflected in the THz spectra (Fig. 7). Very recent neutron studies of the magnetic ordering of Ni_3TeO_6 single crystals have revealed that the commensurately modulated collinear antiferromagnetic structure changes above 8.6 T to an incommensurately modulated conical spiral

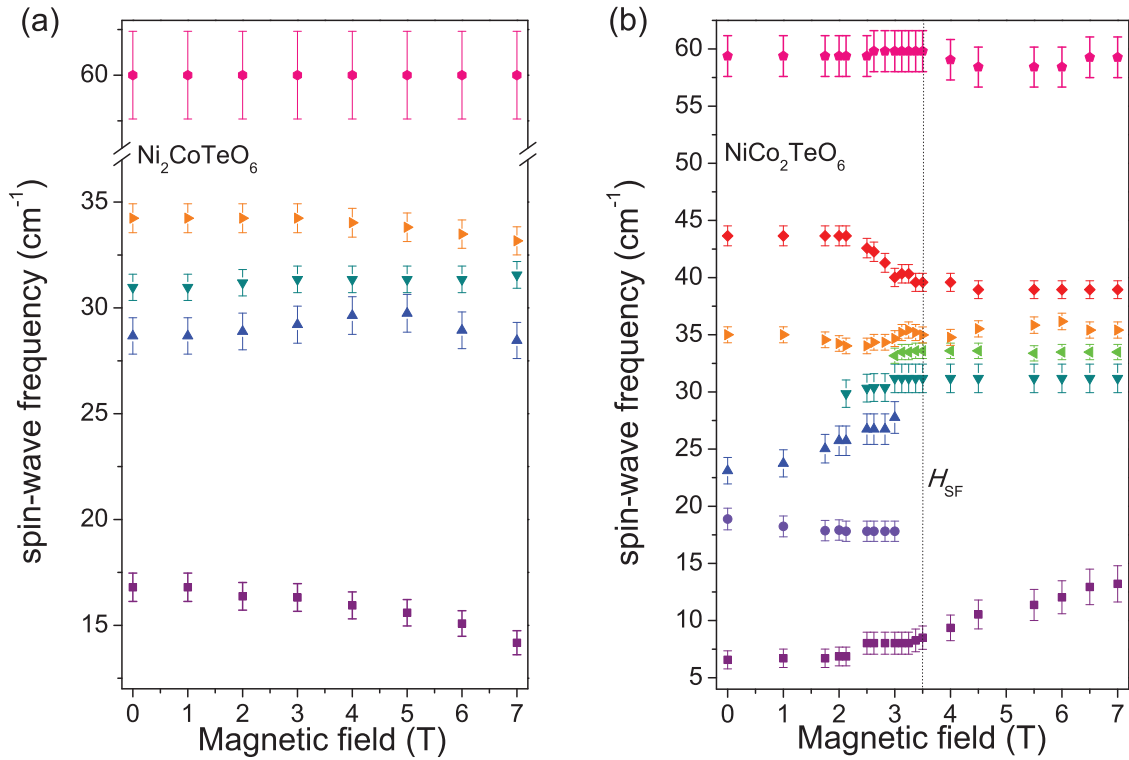FIG. 6. Magnetic field dependence of spin-wave frequencies for (a) Ni_2CoTeO_6 and (b) $NiCo_2TeO_6$, at 5 K. In the latter, the spin-flop transition is clearly seen at approximately 3 T (designated by the violet stripe), by the steps on the magnon branches, as well as both the appearance of new modes and extinction of ones present in the low-field phase.

one with significant spin components in the *ab* plane [33]. One can expect that the THz spectra of Ni_3TeO_6 taken above 8.6 T should resemble the spectra of $NiCo_2TeO_6$ at zero magnetic field. Unfortunately, the magnetic cryostat used for measuring the THz spectra operates up to 7 T. In addition, the absence of evidence of the exact spin order at external magnetic field for all compounds (except for Ni_3TeO_6) and the fact that the THz experiments were performed with polycrystalline samples prevents us from drawing a detailed comparison between compounds.

Large enough single crystals are required for more extensive THz measurements, in order to resolve the relation between crystal symmetry and magnon symmetry and propagation. Also the alternative of studying directional dichroism is currently not feasible due to the small size of the available crystals, and because the pyroelectric polarization is most likely nonswitchable [36]. Finally, single crystals could also

serve for performing pyrocurrent measurements in external magnetic field, in order to examine the static ME coupling, and compare it with the colossal ME effect observed in Ni_3TeO_6.

IV. CONCLUSIONS

New compounds from the family of Ni-based tellurates, Ni_2CoTeO_6 and $NiCo_2TeO_6$, were successfully synthesized in the form of single crystals and ceramics. Co substitution of Ni in Ni_3TeO_6 preserves the ME properties of the parent structure, and it enhances the dynamical ME coupling. The noncentrosymmetric rhombohedral $R3$ structure is maintained at least up to RT for both Ni_2CoTeO_6 and $NiCo_2TeO_6$, even though Co_3TeO_6 has a monoclinic nonpolar structure with the space group $C2/c$. Unfortunately, evidence of ferroelectricity is still missing, since our single-crystalline samples were too

TABLE I. Overview of main characteristics of magnetic phase transitions and spin orders for the $Ni_{3-x}(Co, Mn)_xTeO_6$ ($x = 0-2$) compounds: paramagnetic to AFM phase transition at T_N, spin-flop transition at external magnetic field H_{SF}, type of spin order and spin orientation, and spin order propagation vector k. The metamagnetic phase transitions observed in Ni_3TeO_6 at higher magnetic fields (up to 92 T) [31–33] are not included here.

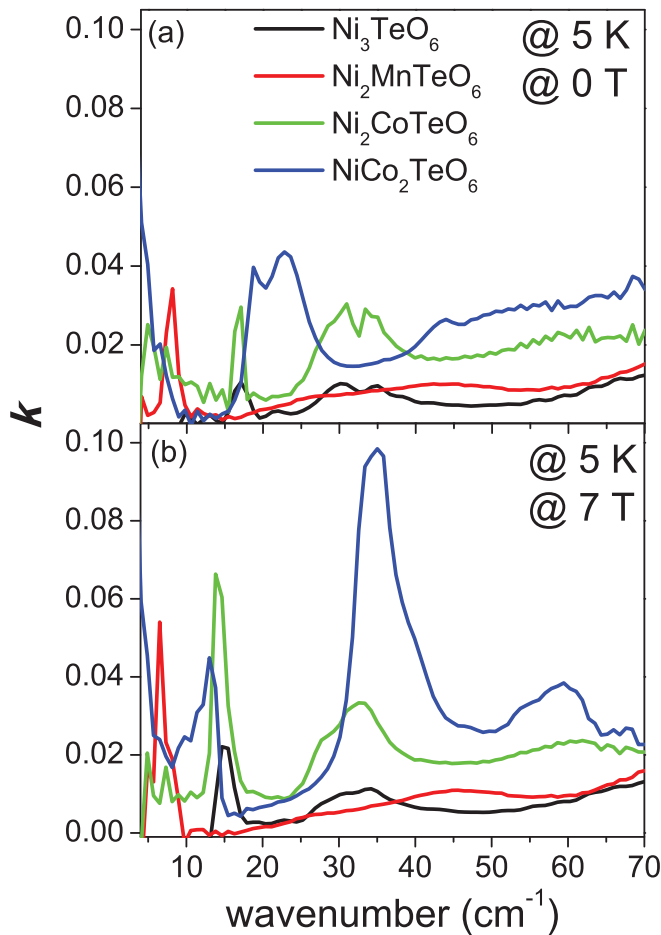|	Ni_3TeO_6 [1,3]	Ni_2MnTeO_6 [6]	Ni_2CoTeO_6	$NiCo_2TeO_6$
T_N (K)	53	70	55	52
H_{SF} (T)	8.2	4.5	8	4
Spin order	collinear *c* axis	collinear *c* axis	helical *ab* plane	helical *ab* plane
k	[0, 0, 0.5]	[0, 0, 0.5]	[0, 0, 1.299(4)]	[0, 0, 1.2109(1)]

FIG. 7. Comparison of THz extinction coefficient spectra k for $Ni_{3-x}(Co, Mn)_xTeO_6$ ($x = 0, 1, 2$) compounds taken at 5 K at (a) zero magnetic field and (b) 7 T.

small for pyrocurrent or ferroelectric hysteresis loops measurements. The magnetic ordering appears in single crystals (ceramics) at $T_N = 55(54)$ and 52 (49) K for Ni_2CoTeO_6 and $NiCo_2TeO_6$, respectively.

In contrast to the magnetic ordering in Ni_3TeO_6 and Ni_2MnTeO_6, which are collinear along the c axis, the two compounds under study present a helical noncollinear structure with the spins in the ab plane. Hysteretic spin-flop transitions were observed in both compounds, near 8 T (Ni_2CoTeO_6) and 4 T ($NiCo_2TeO_6$), in contrast to Ni_3TeO_6 and Ni_2MnTeO_6, which did not show any hysteretic behavior.

Below T_N in the THz range both compounds demonstrate numerous spin excitations, which are markedly influenced by external magnetic field, with clear modifications at the spin-flop transition of $\sim$4 T for the case of $NiCo_2TeO_6$. The Co-richer compound $NiCo_2TeO_6$ prevails, manifesting six magnons unusually strongly dependent on magnetic field. Both compounds present at least one magnetic excitation simultaneously seen by Raman spectroscopy, thus they can be assigned to electromagnons.

[1] Y. S. Oh, S. Artyukhin, J. J. Yang, V. Zapf, J. W. Kim, D. Vanderbilt, and S.-W. Cheong, Nat. Commun. **5**, 3201 (2014).

[2] S. Skiadopoulou, F. Borodavka, C. Kadlec, F. Kadlec, M. Retuerto, Z. Deng, M. Greenblatt, and S. Kamba, Phys. Rev. B **95**, 184435 (2017).

[3] I. Živković, K. Prša, O. Zaharko, and H. Berger, J. Phys. Condens. Matter **22**, 56002 (2010).

[4] V. G. Bar'yakhtar and I. E. Chupis, Sov. Phys. Solid State **11**, 2628 (1970).

[5] A. Pimenov, A. A. Mukhin, V. Y. Ivanov, V. D. Travkin, A. M. Balbashov, and A. Loidl, Nat. Phys. **2**, 97 (2006).

[6] M. Retuerto, S. Skiadopoulou, F. Borodavka, C. Kadlec, F. Kadlec, J. Prokleška, Z. Deng, J. A. Alonso, M. T. Fernandez-Diaz, F. O. Saouma, J. I. Jang, D. Legut, S. Kamba, and M. Greenblatt, Phys. Rev. B **97**, 144418 (2018).

[7] S. A. Ivanov, R. Tellgren, C. Ritter, P. Nordblad, R. Mathieu, G. Andre, N. V. Golubko, E. D. Politova, and M. Weil, Mater. Res. Bull. **47**, 63 (2012).

[8] M. Hudl, R. Mathieu, S. A. Ivanov, M. Weil, V. Carolus, T. Lottermoser, M. Fiebig, Y. Tokunaga, Y. Taguchi, Y. Tokura, and P. Nordblad, Phys. Rev. B **84**, 180404 (2011).

[9] W.-H. Li, C.-W. Wang, D. Hsu, C.-H. Lee, C.-M. Wu, C.-C. Chou, H.-D. Yang, Y. Zhao, S. Chang, J. W. Lynn, and H. Berger, Phys. Rev. B **85**, 094431 (2012).

[10] P. Tolédano, V. Carolus, M. Hudl, T. Lottermoser, D. D. Khalyavin, S. A. Ivanov, and M. Fiebig, Phys. Rev. B **85**, 214439 (2012).

[11] A. B. Harris, Phys. Rev. B **85**, 100403 (2012).

[12] C.-W. Wang, C.-H. Lee, C.-Y. Li, C.-M. Wu, W.-H. Li, C.-C. Chou, H.-D. Yang, J. W. Lynn, Q. Huang, A. B. Harris, and H. Berger, Phys. Rev. B **88**, 184427 (2013).

[13] H. Singh, H. Ghosh, T. V. Chandrasekhar Rao, G. Sharma, J. Saha, and S. Patnaik, J. Appl. Phys. **119**, 044104 (2016).

[14] See Supplemental Material at http://link.aps.org/supplemental/10.1103/PhysRevB.101.014429 for crystal and magnetic structures (XRD and PND data), magnetic studies, additional Raman and THz spectra, table of modes seen in IR and Raman spectra.

[15] G. Kresse and J. Furthmüller, Phys. Rev. B **54**, 11169 (1996).

[16] J. P. Perdew, K. Burke, and M. Ernzerhof, Phys. Rev. Lett. **77**, 3865 (1996).

[17] A. I. Liechtenstein, V. I. Anisimov, and J. Zaanen, Phys. Rev. B **52**, R5467 (1995).

[18] M. O. Yokosuk, A. al-Wahish, S. Artyukhin, K. R. O'Neal, D. Mazumdar, P. Chen, J. Yang, Y. S. Oh, S. A. McGill, K. Haule, S.-W. Cheong, D. Vanderbilt, and J. L. Musfeldt, Phys. Rev. Lett. **117**, 147402 (2016).

[19] M. Rössle, C. N. Wang, P. Marsik, M. Yazdi-Rizi, K. W. Kim, A. Dubroka, I. Marozau, C. W. Schneider, J. Humlíček, D. Baeriswyl, and C. Bernhard, Phys. Rev. B **88**, 104110 (2013).

[20] L. C. Chapon, P. Manuel, P. G. Radaelli, C. Benson, L. Perrott, S. Ansell, N. J. Rhodes, D. Raspino, D. Duxbury, E. Spill, and J. Norris, Neutron News **22**, 22 (2011).

[21] A. Coelho, *Topas Academic: General Profile and Structure Analysis Software for Powder Diffraction Data* (Bruker AXS, Karlsruhe, Germany, 2012).

[22] V. Petříček, M. Dušek, and L. Palatinus, Z. Kristallogr. Cryst. Mater. **229**, 345 (2014).

[23] H. T. Stokes, D. M. Hatch, and B. J. Campbell, ISOTROPY Software Suite, Iso.Byu.Edu (2019).

[24] B. J. Campbell, H. T. Stokes, D. E. Tanner, and D. M. J. Hatch, J. Appl. Crystallogr. **39**, 607 (2006).

[25] F. Gervais, High-Temperature Infrared Reflectivity Spectroscopy by Scanning Interface, in *Infrared Millimeter Waves*, Vol. 8, edited by K. J. Button (Academic, New York, 1983), Chap. 7, p. 279.

[26] M. Tyunina, A. Dejneka, D. Rytz, I. Gregora, F. Borodavka, M. Vondracek, and J. Honolka, J. Phys. Condens. Matter **26**, 125901 (2014).

[27] S. A. Ivanov, R. Mathieu, P. Nordblad, R. Tellgren, C. Ritter, E. Politova, G. Kaleva, A. Mosunov, S. Stefanovich, and M. Weil, Chem. Mater. **25**, 935 (2013).

[28] K. L. Ji, E. Solana-Madruga, A. M. Arevalo-Lopez, P. Manuel, C. Ritter, A. Senyshyn, and J. P. Attfield, Chem. Commun. **54**, 12523 (2018).

[29] Á. M. Arévalo-López, E. Solana-Madruga, E. P. Arévalo-López, D. Khalyavin, M. Kepa, A. J. Dos Santos-García, R. Sáez-Puche, and J. P. Attfield, Phys. Rev. B **98**, 214403 (2018).

[30] R. M. White, R. J. Nemanich, and C. Herring, Phys. Rev. B **25**, 1822 (1982).

[31] J. W. Kim, S. Artyukhin, E. D. Mun, M. Jaime, N. Harrison, A. Hansen, J. J. Yang, Y. S. Oh, D. Vanderbilt, V. S. Zapf, and S.-W. Cheong, Phys. Rev. Lett. **115**, 137201 (2015).

[32] M. O. Yokosuk, S. Artyukhin, A. Al-Wahish, X. Wang, J. Yang, Z. Li, S.-W. Cheong, D. Vanderbilt, and J. L. Musfeldt, Phys. Rev. B **92**, 144305 (2015).

[33] J. Lass, C. Røhl Andersen, H. K. Leerberg, S. Birkemose, S. Toth, U. Stuhr, M. Bartkowiak, C. Niedermayer, Z. Lu, R. Toft-Petersen, M. Retuerto, J. Okkels Birk, and K. Lefmann, arXiv:1909.13734v2 (2019).

[34] M. E. Foglio and G. E. Barberis, Brazilian J. Phys. **36**, 40 (2006).

[35] L. Chaix, S. de Brion, S. Petit, R. Ballou, L.-P. Regnault, J. Ollivier, J.-B. Brubach, P. Roy, J. Debray, P. Lejay, A. Cano, E. Ressouche, and V. Simonet, Phys. Rev. Lett. **112**, 137201 (2014).

[36] X. Wang, F.-T. Huang, J. Yang, Y. S. Oh, and S.-W. Cheong, APL Mater. **3**, 076105 (2015).